JOURNAL OF THE AMERICAN CHEMICAL SOCIETY

Article

Molecular Scaffolding Strategy with Synergistic Active Centers to Facilitate Electrocatalytic CO2 Reduction to Hydrocarbon/Alcohol

Yan Jiao, Yao Zheng, Ping Chen, Mietek Jaroniec, and Shi-Zhang Qiao

J. Am. Chem. Soc., **Just Accepted Manuscript** • DOI: 10.1021/jacs.7b10817 • Publication Date (Web): 19 Nov 2017

Molecular Scaffolding Strategy with Synergistic Active Centers to Facilitate Electrocatalytic CO_2 Reduction to Hydrocarbon/Alcohol

Yan Jiao[1,‡], Yao Zheng[1,‡], Ping Chen[1,2,‡], Mietek Jaroniec,[3] Shi-Zhang Qiao[1,4]*

[1] School of Chemical Engineering, The University of Adelaide, Adelaide, South Australia 5005, Australia

[2] School of Chemistry and Chemical Engineering, Anhui University, Hefei, P. R. China

[3] Department of Chemistry and Biochemistry, Kent State University, Kent, Ohio 44242, USA

[4] School of Materials Science and Engineering, Tianjin University, Tianjin 300072, China

ABSTRACT: A major impediment of the electrocatalytic CO_2 reduction reaction (CRR) is the lack of electrocatalysts with both high efficiency and good selectivity toward liquid fuels or other valuable chemicals. Effective strategies for the design of electrocatalysts are yet to be discovered to substitute the conventional trial-and-error approach. This work shows that a combination of the density functional theory (DFT) computation and experimental validation on molecular scaffolding to coordinate the metal active centers presents a new molecular-level strategy for the development of electrocatalysts with high CRR selectivity toward hydrocarbon/alcohol. Taking the most widely investigated Cu as a probe, our study reveals that the use of graphitic carbon nitride (g-C_3N_4) as a molecular scaffold allows for an appropriate modification of the electronic structure of Cu in the resultant Cu-C_3N_4 complex. As a result, adsorption behavior of some key reaction intermediates can be optimized on the Cu-C_3N_4 surface, which greatly benefits the activation of CO_2 and leads to a more facile CO_2 reduction to desired products as compared with those on the Cu(111) surface and other kinds of Cu complexes formed on nitrogen-doped carbons. Remarkably, different from the most studied elementary metal surfaces, an intramolecular synergistic catalysis with dual active centers was for the first time observed on the Cu-C_3N_4 complex model, which possesses unique capability for the generation of C2 products. A good agreement between electrochemical measurements and the DFT analysis of CRR has been achieved based on the newly designed and synthesized Cu-C_3N_4 electrocatalyst.

INTRODUCTION

Carbon dioxide reduction reaction (CRR) by electrocatalysis holds a great promise to produce sustainable carbon-based fuels from renewable resources.[1] With the input from sustainable energy such as solar and wind, this energy conversion process utilize carbon as an energy carrier to produce fuels, addressing the storage issues of the often intermittent resources.[2] Because of the inert nature of CO_2 molecule, this normally exothermic process is naturally difficult to proceed and is greatly dependent on the careful selection of highly active electrocatalysts.[3] Additionally, due to the complexity of the charge transfer process occurred in CRR, a wide variety of products is accessible including carbon monoxide (CO) and formic acid (HCOOH) *via* a two-electron reduction pathway, methanol (CH_3OH) *via* six-electron reduction, and methane (CH_4) *via* a complete eight-electron reduction.[4] Practically, the best solution remains the conversion of CO_2 to CH_3OH or, further to C2 products like ethylene (C_2H_4) and ethanol (C_2H_5OH) , as thus the established fuel-transporting infrastructure could be well utilized.[5] However, the availability of suitable electrocatalysts is still very limited.[6] Generally, the selectivity of different reduction products strongly depends on both extrinsic physical properties and intrinsic electronic structure of the heterogeneous electrocatalyst used, which always act together in determining the adsorption of intermediates and activation energies for each reaction.[7] This complexity makes the rational design of suitable electrocatalysts for desired CRR products a great challenge. Therefore, exploration of atomic level understanding of the overall CRR mechanism is highly desired.

Until now, Cu-based materials remain to be the most efficient and selective CRR electrocatalysts providing a wide variety of products depending on their chemical and/or physical properties.[8] The density functional theory (DFT) computational studies of these catalysts revealed that their great performance can be related to the appropriate adsorption strength of key reaction intermediates.[9] Therefore, the design and engineering of Cu-based catalysts with suitable electronic structure to achieve wider product distribution and/or higher selectivity is still the mainstream research direction for CRR. Current strategies to engineer Cu catalysts are mainly relying on the modification of their physical structure and/or chemical composition by straightforward methods. However, due to the complex nature of CRR and the aforementioned complicated relationship between the apparent activity/selectivity of a given electrocatalyst and its inherent adsorption energetics toward key intermediates, almost all of the current approaches toward development of CRR electrocatalysts are still *via* a trial-and-error method; an atomic scale design strategy is largely missing.

Due to the ability of transition metals to form coordination complexes with ligands, coordinating Cu into molecular frameworks could provide a platform for engineering novel Cu-based CRR electrocatalysts with unprecedented properties.[10] Previously, based on both theoretical and experimental studies we showed that coordinating a range of transi-

tion metals (*e.g.,* Fe, Co, Ni) into the framework of graphitic carbon nitride (g-C_3N_4) can introduce excellent electrocatalytic activities toward two key oxygen electrode reactions (oxygen reduction/evolution reactions) for fuel cells and water splitting applications.[11] A strong coordinating capability and particular functional species of g-C_3N_4 framework make it a suitable new platform for efficient metal coordination instead of traditional nitrogen-doped carbons. As regards CRR, in principle, g-C_3N_4 possesses at least two particular properties that differs it from other nitrogen-containing carbon substrates. First, the abundant pyridinic nitrogen species in g-C_3N_4 framework show strong affinity to CO_2 under electrocatalytic conditions, which is considered critical for CO_2 activation.[12] Second, carbon species in g-C_3N_4 show high oxophilicity for adsorption of oxygen-containing reaction intermediates (*OCH_x, *OH, and *O) during CRR, which appear in the second half of the reaction pathway, benefiting the generation of deep reduction products.[13] Therefore, g-C_3N_4 could serve as an ideal molecular scaffold for Cu to form Cu-C_3N_4 structure for efficient and effective CRR.

In this work, we explored different CO_2 reduction pathways on Cu-C_3N_4 structures (for comparison, we also studied Cu supported on nitrogen-doped graphene named as Cu-NC)[14], by investigating a full range of possible reaction intermediates. According to the thermodynamic analysis, Cu-C_3N_4 shows two unique and critical features for CRR as compared with Cu(111) surface and other kinds of nitrogen-containing carbons with coordinated Cu complexes. First, g-C_3N_4 can influence copper's electronic structure by shifting its d-band position toward Fermi level, therefore leading to a stronger adsorption of intermediates and smaller energy loss toward hydrogenation of CO_2. Second and more importantly, different from the widely studied bifunctional catalysts composed of a metallic site and a support for CO/CO_2 conversion,[15] Cu-C_3N_4 shows an intramolecular synergistic effect toward CRR, where Cu and C act in synergy for different stages of the reaction. As a result, an enhanced CO_2 reduction to C2 species (*e.g.*, C_2H_5OH and C_2H_6) was achieved in Cu-C_3N_4 system due to the unique dual active center synergistic catalysis. This thermodynamic-based theoretical prediction was further validated by electrochemical measurements performed on experimentally synthesized Cu-C_3N_4 catalysts, which showed a wider variety of C2 products (C_2H_5OH, C_2H_6, and C_2H_4) and higher selectivity of deep reduction products (CH_4 and CH_3OH) in comparison to conventional Cu-NC counterparts.

METHODS

Computational Methods and Models. Electronic structure calculations were carried out by DFT with Perdew-Burke-Ernzerhof (PBE) exchange-correlation functional using a projector augmented-wave method by VASP code.[16] For the plane-wave expansion, a 500 eV kinetic energy cut-off was used after testing a series of different cut-off energies. The convergence criterion for electronic structure iteration was set to be 10^{-5} eV and that for geometry optimization was set to be 0.01 eV/Å. A Gaussian smearing of 0.20 eV was applied during the geometry optimization and for the total energy computations, whilst for the accurate density of states (DOS) computation a tetrahedron method with Blöchl correction was employed. The K-points were set to be 5×5×1 for the Cu-C_3N_4 unit cell, 3×3×1 for graphene-based Cu-NC model. Denser K-points were used for the high quality DOS computations (15×15×1 for Cu-C_3N_4, and 9×9×1 for Cu-NC). The Tkatchenko-Scheffler method was applied during all calculations to properly address the van der Waals interactions between atoms.[17]

Three surface models were studied in this work: Cu-C_3N_4, Cu-NC, and Cu(111) (for the purpose of comparison). For Cu-C_3N_4, the lattice parameters used were 7.089Å × 7.089Å × 20Å, with the angle between the first two vectors being 120°. The Cu-NC model was based on a 5×5 graphene supercell, and the lattice was optimized to be 12.329Å × 12.329Å × 20Å. For copper single crystal, the lattice constant was optimized to be 3.551Å, while the DOS computation was carried out for a four layer slab model in the [111] direction, with 15Å space between two slabs. The atomic configuration and electron charge transfer due to the incorporation of copper to Cu-C_3N_4 and Cu-NC are shown in Figure S1 (supporting information). Bader charge analysis shows that the electron transfers from the embedded copper atom to g-C_3N_4 (0.751 e^-) or nitrogen-doped graphene (0.929 e^-) frameworks.

Reaction Intermediates. First, the CO_2 adsorption on Cu-C_3N_4 was investigated because this is the first step that occurs during CRR. The adsorption location and pattern often give useful information about reaction steps, for example the potential active sites. As shown in Figure S2, various positions for CO_2 adsorption were investigated and the possible adsorption sites are listed. CO_2 molecule prefers to adsorb on copper and nitrogen atoms rather than on carbon atoms. Specifically, a 'mock chemisorption' exists on nitrogen atom, where CO_2 is adsorbed on Cu-C_3N_4 *via* a carbon-nitrogen bond (Figure S2f), indicating the ability of Cu-C_3N_4 toward activating CO_2 if proper electrode potential is applied.[12a] The formation of this configuration could be attributed to the electron accumulation on nitrogen due to its higher electronegativity than that of surrounding carbon atoms. The search for all other possible reaction intermediates (*COOH, *CO, *COH, *CH *etc.*, see Table S1 and S2 for the complete list of investigated states and corresponding relative stability) on Cu-C_3N_4 and Cu-NC also begins with various different initial configurations. The free energy corrections to each state are presented in Table S3 (for adsorbed states) and Table S4 (for gas phase properties). The free energy diagram of CO_2 reduction on Cu(111) is taken from reference 18. Equilibrium potentials of several key CRR products are summarized in Table S5.

Sample Synthesis and Characterization. To match the models proposed in the computation, the synthesis of Cu-C_3N_4 nanomaterials was conducted by mixing different amounts of $CuCl_2$ aqueous solutions with dicyandiamide (DCDA) in room temperature. For instance, 1.3, 2.5, 4.8, and 10 mL of 0.1 M $CuCl_2$ solution with 0.66, 0.64, 0.60, 0.54 g of DCDA and 10 mL of water were selected to prepare the sample with theoretical ratio of Cu: C_3N_4 = 1:20, 1:10, 1:5, 1:2, respectively. Different ratios were chosen to assure Cu ion coordination with g-C_3N_4 as efficient as possible. 50% mass concentration of acid pretreated carbon black was applied at the same time as a support to enhance the electrode conductivity and to expose the electrocatalytically active sites of Cu-C_3N_4. After stirring overnight, the mixture was lyophilized and annealed at 600 °C in N_2. The powder was subsequently washed twice with 1M HNO_3 and then several times with water to remove uncoordinated copper/copper oxide particle. The synthesis of Cu-NC was carried out by annealing the after-washed Cu-C_3N_4 sample at 900 °C in N_2, during which the molecular scaffold of g-C_3N_4

was decomposed and converted to nitrogen-doped carbon with bonded Cu.

The near edge X-ray absorption fine structure (NEXAFS) and X-ray photoelectron spectroscopy (XPS) measurements were carried out on soft X-ray spectroscopy beamline at the Australian Synchrotron. In all NEXAFS scans, 50 meV energy steps were used. In the XPS scans, the excitation energy was 700 eV for better signal-to-noise ratio and the E-pass was set to 5 eV for optimum energy resolution. The transmission electron microscopy (TEM) was carried on FEI Tecnai G2 Spirit TEM operated at 120 kV.

Electrochemical Measurements and Product Analysis. The evaluation of CRR performance on two synthesized samples were done using a homemade H-type cell with two compartments separated by the Nafion membrane. Each compartment contains 50 mL of electrolyte (0.1 M $KHCO_3$) and about 50 mL headspace. The measurements were carried out using CHI 750E electrochemical workstation at room temperature. The electrocatalysts were loaded on the glassy carbon serving as working electrode. A Pt plate and an Ag/AgCl in saturated KCl solution were used as counter and reference electrodes, respectively. Before each measurement, the cathodic compartment of the cell was degassed and saturated with CO_2 at 40 mL/min for at least 20 min. During the reduction, CO_2 gas was continuously bubbled into the cathodic compartment. The gaseous products were delivered directly to the sampling loop of an on-line gas chromatograph equipped with a thermal conductivity detector using Ar as a carrier gas for H_2 analysis and a flame ionization detector for CO, CH_4, C_2H_4, and C_2H_6 analysis. The liquid products (*e.g.* HCOOH, CH_3OH, and C_2H_5OH) were detected by NMR (Bruker 400 MHz).

RESULTS AND DISCUSSION

Reaction Pathway. We obtained the configurations of all possible reaction intermediates and their corresponding free energies by DFT computations. Afterwards the lowest energy reaction pathway – defined to be the pathway with lowest positive elementary free energy change between any two steps – toward CH_4 production is summarized in Figure 1a. In this figure, the x-axis represents the transferred numbers of proton/electron pairs to the electrode surfaces including Cu-C_3N_4, Cu-NC, and traditional Cu(111) slab. Generally, the first few reduction steps of CO_2 to CH_4 on these three surfaces follow the same pathway, which starts with hydrogenation of an adsorbed *CO_2 to form *COOH. Following the OH desorption, a *CO is left on the surface and the second protonation process occurs to form *CHO. These two protonation processes are traditionally considered as the rate-limiting-steps of CO_2 reduction; for example, on the Cu(111) slab surface, 0.9 and 0.8 eV free energy change could be observed for CO_2 and *CO hydrogenation, respectively.[18] Meanwhile, on the Cu-C_3N_4 surface, due to the lower free energy level of the state after the first hydrogenation step (*COOH), the second hydrogenation process (*CHO) becomes the only rate-limiting-step. The free energy change of this step is 0.75 eV uphill, less endothermic than on Cu(111) slab surface. As for the Cu-NC surface, the free energy change of the first hydrogenation step is higher than that of the second one, with values of 1.34 eV and 0.44 eV, respectively, and therefore the first protonation is considered as the major reaction rate-determining step.

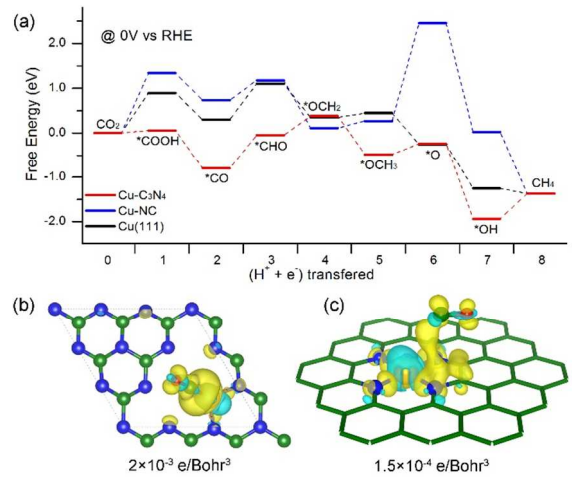

Figure 1 (a) Free energy diagram of CO_2 reduction pathway to CH_4 on Cu-C_3N_4, Cu-NC, and Cu(111). The values for the Cu(111) surface are taken from reference 18. Electron density difference for CO adsorbed on (b) Cu-C_3N_4 and (c) Cu-NC. The unit of isosurface values is shown in the figure. Green, blue, gold, and red atoms are carbon, nitrogen, copper and oxygen, correspondingly. Yellow is electron accumulation and cyan represents electron depletion.

Though the first four-electron transfer steps proceed with identical reaction intermediates on three copper-embedded surfaces, the reaction pathway starts to diverge when the fifth proton and electron pair is transferred to the surface. In the case of Cu-C_3N_4 and Cu(111), an *OCH_3 group is formed with oxygen as an anchoring atom on the surface of the aforementioned catalysts, followed by the formation of an isolated CH_4 molecule and adsorbed *O after the sixth proton/electron pair transfer. As for the reduction pathway on the Cu-NC surface, the fifth step includes the generation of *CH_2OH, followed by OH desorption to form *CH_2 and therefore two steps of hydrogenation are needed to produce CH_4 after the last proton/electron pair transfer, as shown in Figure S3b, blue line. On this pathway, all free energy changes from 2nd to 8th charge transfer process on Cu-NC are smaller than that for the first charge transfer, therefore the rate-determining step is the protonation of CO_2 to *COOH. For the purpose of comparison, Figure 1a depicts the same CRR pathway to CH_4 on all three surfaces. Despite of the different reduction pathway on the three electrocatalysts, Cu-C_3N_4 generally shows the strongest binding to reaction intermediates and therefore the lowest free energy pathway.

Following reference 9f we have also examined an alternative reaction pathway for CH_4 production on Cu-C_3N_4 and Cu-NC. For the two evaluated pathways on Cu-C_3N_4, as shown in Figure S3a, the first half of these pathways (until the forth proton/electron pair transfer) is the same as discussed in the previous paragraph. The main pathway (black line) involves the protonation of *CHO to form *OCH_2 with the upcoming hydrogen connecting the carbon atom, with a free energy change of 0.43 eV for this step. An alternative reaction pathway (red line) involves a different reaction intermediate following *CHO, where the upcoming hydrogen is connected to O and forms *CHOH. The free energy change for this intermediate state is 0.74 eV, higher than the previously mentioned pathway. The remaining part of this alternative pathway is OH desorption to form adsorbed *CH, followed by three steps of hydrogenation and the final CH_4 production. For the Cu-NC

surface, as shown in Figure S3b, the alternative reaction pathway considered in reference 9f (red line) is also higher in energy than the lowest possible pathway (blue line). Therefore, the above-mentioned pathways are higher in the free energy and are thermodynamically unfavorable.

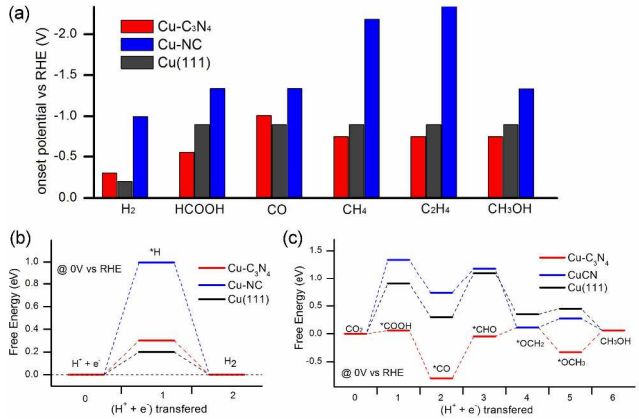

Figure 2 (a) Summary of the onset potential of the products of CO_2 reduction as predicted by the reaction free energy diagrams on three different surfaces. Detailed free energy diagram of (b) hydrogen evolution and (c) CO_2 reduction to CH_3OH on three copper-based surfaces.

To explain the lower free energy possessed by reaction intermediates on Cu-C_3N_4 in comparison to that on Cu-NC, the electron density difference analysis was carried out using *CO adsorption as an example. As regards the Cu-C_3N_4 surface, at an isosurface cut-off of 2×10^{-3} e/Bohr^3, electron transfers from the copper present in Cu-C_3N_4 and the carbon atom (from CO molecule) to the Cu-C bonding area between these two moieties, suggesting a strong interaction between these two parts (Figure 1b). As a result, the CO triple bond weakens as indicated by the electron depletion alongside the bond, with its length stretched from 112.8 pm to 115.6 pm (comparable to a CO double bond). Additionally, CO-Cu bond length within this configuration is 1.77 Å. While in striking contrast to the Cu-NC surface, the distance between carbon on CO and nitrogen as the adsorption center is 3.42 Å, much longer than that on Cu-C_3N_4. A significant charge transfer between Cu-NC framework and CO is only visible at an isosurface value of about 1.5×10^{-4} e/Bohr^3, about one magnitude lower than that on Cu-C_3N_4 (Figure 1c). At the meantime the CO bond length is 114.4 pm. These considerations show the strong adsorption CO on Cu-C_3N_4 and very weak one on Cu-NC, which leads to the much lower free energy level for the CO-containing reaction intermediates as well as other reaction intermediates.

Onset Potential. When considering the full methane pathway, the smallest negative potential at which the pathway becomes exergonic (*i.e.,* the limiting potential) for Cu-C_3N_4, Cu-NC and Cu(111) is 0.75 V, 2.18 V, and 0.90 V respectively. This phenomenon, therefore suggests a better catalytic activity of Cu-C_3N_4 toward CO_2 reduction to methane when using limiting potential as an activity descriptor. The limiting potential toward other products including H_2, CH_3OH, HCOOH, CO, and C_2H_4, are summarized in Figure 2 (a). Generally, Cu-C_3N_4 shows lowest required potential among the three surfaces to open pathways toward deep reduced products, which indicates smaller electrical energy loss and therefore higher efficiency in generating these products. In comparison, the overpotential required to produce CO on Cu-C_3N_4 is higher than Cu(111), which suggests worse activity possessed by Cu-C_3N_4. Meanwhile, Cu-NC shows significantly high limiting potential toward all products, requesting higher overpotential to kick-start the reactions and therefore poorer performance from the computational point of view.

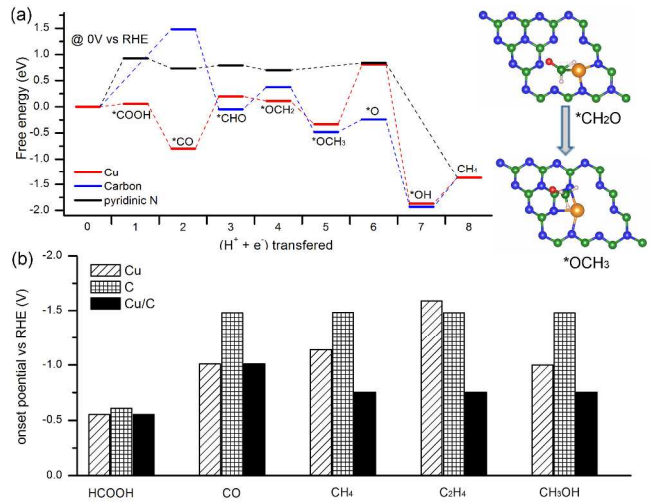

Figure 3 (a) Free energy diagram of CO_2 reduction to CH_4 on different sites of Cu-C_3N_4. Inset shows the migration of active center from Cu to carbon. (b) Summary of the onset potential of the products of CO_2 reduction as predicted by the reaction free energy diagrams on different sites of Cu-C_3N_4. Smaller value indicates the lower onset potential required, hence better performance of this catalyst.

The detailed free energy diagrams that were used to obtain the aforementioned limiting potentials toward several products are shown in Figure 2 (b: H_2 – *via* hydrogen evolution reaction and c: methanol) and Figure S4 (HCOOH, CO, and C_2H_4). As indicated by these plots, the free energy levels of all reaction intermediates on Cu-C_3N_4 are generally lower than those on other two substrates, except for hydrogen evolution. Since the hydrogen adsorption energy on Cu-C_3N_4 is higher than that on Cu(111), a weaker hydrogen evolution ability of this material should be expected. In contrary to the g-C_3N_4 framework itself, which shows a strong binding to H*, the hydrogen adsorption free energy level is elevated and could be attributed to the copper atom that is already occupying the triangular vacancy formed by surrounding *s*-triazine units. This feature would be particularly beneficial for the production of hydrocarbons, since hydrogen evolution reaction is the major competing reaction with CRR.[19] Additionally by comparing the onset potential required for the generation of formic acid and carbon monoxide, the CO production requires higher overpotential than that of HCOOH, indicating lower selectivity toward CO. This difference is originated by a strong *CO adsorption on Cu-C_3N_4, which makes the CO desorption difficult to proceed.

Dual Active Center Mechanism. During the exploration of all possible reaction pathways on Cu-C_3N_4 toward CH_4 production, various sites were investigated. Generally, the binding of reaction intermediates during the first half of the reaction shows stronger adsorption on the copper atom than on carbon and nitrogen sites of the Cu-C_3N_4 substrate. Meanwhile during the latter half of the reaction, the reaction intermediates show stronger binding to the carbon site than on the copper site. Therefore, the lowest free energy pathway toward CH_4 production is given when these two sites are both considered

as a dual-active site. As shown in Figure 3a, the dual active site pathway leads to an overall limiting potential of 0.75 V. It is worth noting that the limiting potential toward CH_4 production when considering Cu as the only active center for the whole reaction is 1.14 V, while that for the carbon as the sole active center is 1.48 V, both higher than the dual-active site pathway. The inset shows transfer of active center, which illustrate the synergistic effect of Cu and g-C_3N_4 framework. The origin of this behavior is that copper shows strong binding to reaction intermediates having carbon as an anchoring atom (*e.g.* *COOH, *CO, *CHO), while the carbon on g-C_3N_4 shows stronger binding to reaction intermediates having oxygen as the connecting atom (*e.g.* *OCH2, *OCH3, *O, and *OH). Therefore, during the first half of the reaction, reaction intermediates favor copper-carbon bond; while during the latter half of the reaction, the reaction intermediates are connected to the surface via a carbon-oxygen bond. We have also quantitatively analyzed the limiting potential toward other products, as shown in Figure 3b, and observed the same behavior. Therefore, the unique structure of metal coordinated by g-C_3N_4 framework leads to a synergistic reaction scheme that leads to a more feasible reaction pathway induced by the migration of active center.

Inspired by this observation that Cu atom serves as the active center for carbon (and C-containing groups) adsorption, while the adjacent carbon atom on g-C_3N_4 serves as the active center for reaction intermediates having oxygen as the connecting atom, we further explored the possibility of C_2 pathway on Cu-C_3N_4. Here we present the free energy pathway of CO_2 reduction to CH_3CH_2OH as an example, as shown in Figure S5. The first five proton/electron transfers follow the same pathway as that shown in Figure 1a, forming an adsorbed *OCH_3 group on the carbon atom. Where starting from the sixth proton/electron pair transfer, the second CO_2 adsorbs on the copper atom along with a protonation process. The configuration of consequently occurring reaction steps is shown in Figure 4, where the second *COOH undergoes a series of changes to form *CH_3O on the copper atom. From that point, a bond forms between the two carbon- containing moieties to form CH_3CH_2OH, leaving the surface adsorbed oxygen atom, which is then protonated to form H_2O. The existence of this reaction pathway is due to the molecular scaffold coordinating copper; the unsymmetrical feature of Cu-C_3N_4 could lead to the C2 pathway and therefore, deep reduced products. Correspondingly, the following experimental electrochemical measurements also validate that Cu-C_3N_4 can produce more C2 species like C_2H_6, CH_3CH_2OH than the Cu-NC sample with single active centers under the same condition.

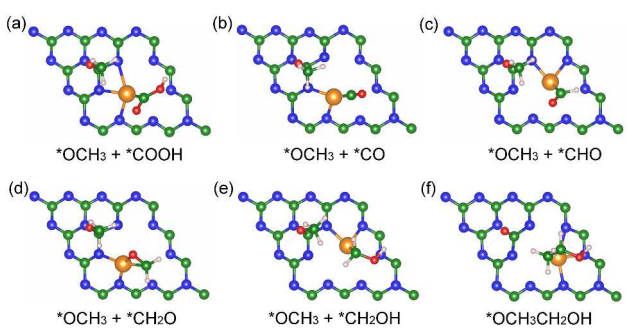

Figure 4 Key reaction intermediates of CH_3CH_2OH generation on Cu-C_3N_4.

Origin of the Activity. In accordance to the above discussion, a linear relationship can be observed between the *COOH and *CO adsorption strengths, as shown in Figure S6a, suggesting that the CO_2 activation ability is proportional to CO adsorption on these three surfaces. As indicated in the aforementioned figure, the CO_2 activation ability possessed by Cu on Cu-C_3N_4 is the highest among the three catalysts, indicating a strong interaction between carbon and the copper atom. This observation also suggests that similar to the scaling relationship between different metals, a counterpart relation exists for the same metal species (for example, copper as shown in this work) when embedded within different frameworks. The underlying reason for this scaling relationship, as well as why Cu-C_3N_4 possesses the strongest CO binding strength, could be unveiled by density of states (DOS) analysis performed on the three surfaces. Figure S6b shows the copper d-orbital density of states on three surfaces, which is considered to play a determining role in interactions with surface adsorbates. The distribution of states shifts toward the higher energy region following the order of Cu-NC → Cu(111) → Cu-C_3N_4, which is consistent with the observed order of the binding energy strength, as shown in Figure S6c. The general trend is that with a higher d-band position such as Cu-C_3N_4, a stronger adsorption is observed due to up-shifting the anti-bonding state, which leads to lower occupation (of the anti-bonding state), and results in weaker repulsion between these two parts.

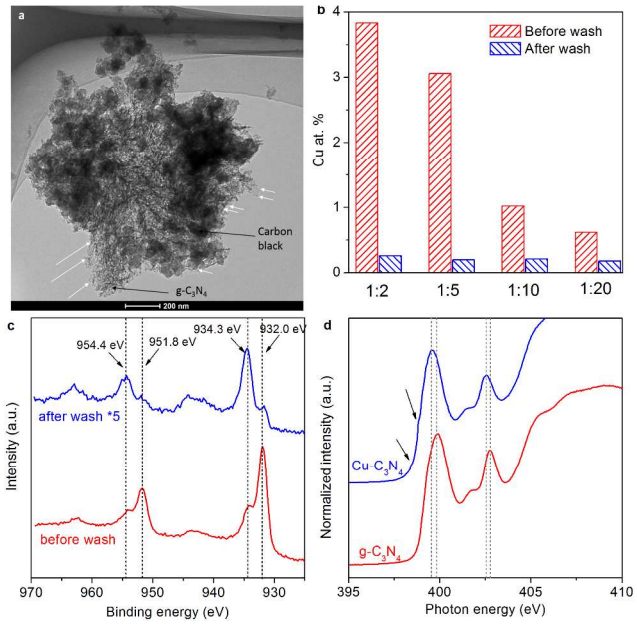

Figure 5 (a) TEM image of typical Cu-C_3N_4 electrocatalyst supported on carbon black. Arrows indicated atomic Cu clusters. (b) Comparison of Cu concentrations in different Cu-C_3N_4 samples before and after acid wash. (c) High resolution Cu^{2p} XPS of Cu-C_3N_4 before and after acid wash. (d) Nitrogen K-edge NEXAFS of Cu-C_3N_4 and pure g-C_3N_4. Arrows show the weak shoulders in N K-edge assigning to the Cu-N interaction. Dotted lines show the channels of photon energy in two samples.

Experimental Validation. To further provide experimental evidence of g-C_3N_4 scaffold's unique role in the CRR process revealed by theoretical calculations, we carried out the synthesis of Cu-C_3N_4 and Cu-NC electrocatalysts with similar molecular structures as investigated theoretically (see details

in experimental section). During the thermal treatment, DCDA was polymerized into g-C_3N_4 scaffold and simultaneously coordinated with Cu ions (Figure 5a). After acid washing, all four samples with different amounts of Cu precursors showed similar Cu atomic concentration in the Cu-C_3N_4 hybrid (Figure 5b), indicating that there is a saturated coordinating ability of g-C_3N_4 scaffold to metal ions. Taking the 1:5 sample as an example, after double nitric acid washing, the Cu concentration in Cu-C_3N_4 decreased from 3.1 to 0.2 at.% with almost unchanged N concentration based on the XPS analysis. (Figure S7). This can be explained by the fact that most Cu in freshly synthesized product is in the form of Cu(0) metal nanoparticles, which can be eliminated by washing with acid solutions. Meanwhile, the remaining Cu species are in the form of single atoms and clusters bonded with nitrogen atoms in the g-C_3N_4 scaffold (Figure 5c,d). As can be seen from the high-resolution XPS data, these Cu species possess higher binding energies than the Cu nanoparticles. The higher valance states of Cu may be attributed to its interaction with g-C_3N_4 in the form of electron transfer from copper to nitrogen atoms (Figure 5c). At the same time, by comparing with the pure g-C_3N_4, the extra weak shoulders in nitrogen K-edge NEXAFS spectrum of Cu-C_3N_4 also indicate nitrogen atoms, more specifically, the pyridinic nitrogen in the triazine heterorings, able to accept extra charges from Cu atoms, which results in a slightly negative shift in its photon energy profile (Figure 5d). Therefore, analysis of Cu 2p XPS and N K- edge NEXAFS spectra confirms that there is a strong chemical interaction (or bonds) between Cu and N atoms in the synthesized Cu-C_3N_4 sample, which match the molecular configuration used in the theoretical computation (Figure S1 in supporting information). It is worth noting that the atomic ratio of Cu and N in all four samples is around 0.0073~0.0091, which is equal to the ratio of tri-s-triazine units to Cu of 8.6 to 11.4 (theoretical value should be 1). This means that not all vacancies in the g-C_3N_4 framework are saturated by Cu species; most of them are still in the pristine form of g-C_3N_4.

The CRR activity/selectivity differences in the synthesized Cu-C_3N_4 and Cu-NC electrocatalysts were analyzed to validate the theoretical considerations. As shown in Figure 6a, the Cu-C_3N_4 sample features a more positive onsite potential and higher current density under a certain overpotential than Cu-NC. Additionally, the Cu-C_3N_4 electrocatalyst was stable during at least 18 hours operation (Figure 6b). The gaseous and liquid products analysis showed that the major product of both Cu-C_3N_4 and Cu-NC electrocatalysts is still hydrogen gas (>50 %) *via* the competitive cathodic hydrogen evolution reaction. This can be explained by the fact that there is a large amount of un-coordinated g-C_3N_4 in the hybrid, which is relatively active to the hydrogen evolution but inert for CRR, according to the theoretical analysis (Figure 3a). Therefore, the real number of active sites on the Cu-C_3N_4 material studied is much lower than that on polycrystalline Cu electrode, which means that the newly developed Cu-C_3N_4 needs further improvement (*e.g.,* advanced synthetic methods) to enhance its potential performance as theoretically predicted.

As a probing model, indeed, Cu-C_3N_4 showed a wider variety of deep reduction products and higher Faradic efficiency for each product under the same potential than the Cu-NC control sample. For example, CH_3OH and CH_4 after 6 and 8 electron transfers were only generated on the Cu-C_3N_4 electrode (Figure 6c, d), due to the lower overall free energy difference as indicated by the free energy diagram (Figure 1,2). More strikingly, Cu-C_3N_4 samples demonstrate the ability of generating C2 species like C_2H_5OH, C_2H_4, and C_2H_6, which is attributed to the unique dual active center mechanism by the special configuration of Cu atom embedded in g-C_3N_4 scaffold (Figure 4). These trends serve as a good agreement between experimental measurement and the thermodynamic-based DFT study of these materials.

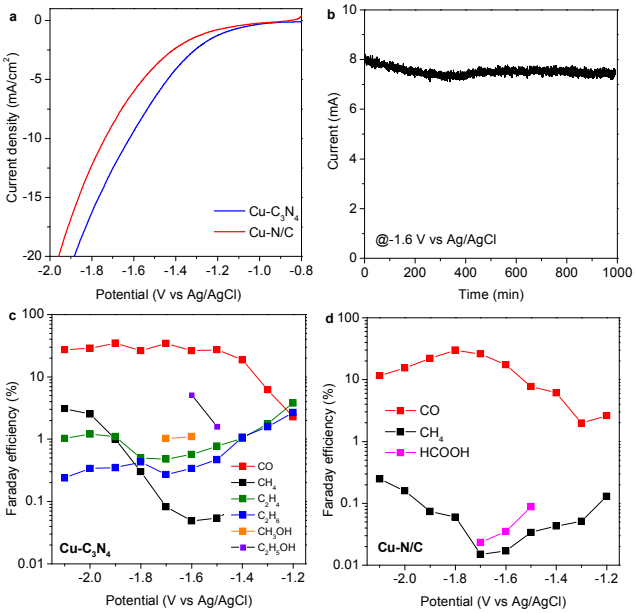

Figure 6 (a) Polarization curves of CO_2 reduction on two electrocatalysts, recorded in CO_2-satuated 0.1 M $KHCO_3$. (b) Stability test of CO_2 reduction on Cu-C_3N_4 electrocatalyst. (c,d) The measured Faradic efficiencies of various products on Cu-C_3N_4 (c) and Cu-NC (d) electrodes under different overpotentials.

CONCLUSION

In summary, we have showed, from both theoretical and experimental perspectives, that for multistep electrochemical reactions like CRR, a particular molecular scaffold facilitating coordination of the metallic centers can play a significant role in affecting the activity and selectivity toward desired reactions. We conducted extensive DFT computations for a Cu-C_3N_4 model catalyst to evaluate its potential for CO_2 reduction, and compared its performance with that of the Cu (111) surface and conventional Cu-NC complex. Based on the computation and experimental results, Cu-C_3N_4 shows significantly better CO_2 reduction activity with lower on-set potential, as well as a significantly higher C2 production rate than that obtained for Cu-NC. Our study reveals that the molecular scaffold can serve as an additional active center for CRR, leading to the synergistic effect for pathways that leads to deep reduced products. This new dual active center model, which has been validated by our experimental measurements, has never been observed in the reported CRR electrocatalyst systems. Additionally, the g-C_3N_4 framework could efficiently uplift copper's d-band position toward Fermi level, which is critical in strengthening the adsorption strength of reaction intermediates and CO_2 activation. Our investigation suggests that selecting appropriate molecular scaffold can be critical to increase the electrocatalytic CO_2 reduction activity. This atomic level finding could be helpful to find more efficient and effective CRR electrocatalysts, and could also be extended to other mul-

ti-electron electrocatalytic reactions like nitrogen reduction reaction for electrochemical ammonia synthesis, oxygen reduction/evolution reactions, and alcohol oxidation reactions.

ASSOCIATED CONTENT

Supporting Information. Detailed computational models, configurations of reaction intermediates, more reaction pathways; more information on materials synthesis, characterization methods, and electrochemical characterization. This material is available free of charge via the Internet at http://pubs.acs.org.

AUTHOR INFORMATION

Corresponding Author

*s.qiao@adelaide.edu.au

Author Contributions

‡These authors contributed equally.

Notes

The authors declare no competing financial interests.

ACKNOWLEDGMENT

We acknowledge financial support by the Australian Research Council (DP170104464, DP160104866, DP140104062, DE160101163 and FL170100154). DFT computations within this research was undertaken with the assistance of resources and services from the National Computational Infrastructure (NCI), which is supported by the Australian Government. NEXAFS and XPS were performed on soft X-ray beamlines at Australian Synchrotron.

REFERENCES

(1) (a) Gattrell, M.; Gupta, N.; Co, A., *J. Electroanal. Chem.* **2006,** *594*, 1; (b) Zhu, D. D.; Liu, J. L.; Qiao, S. Z., *Adv. Mater.* **2016,** *28*, 3423; (c) Chen, Y.; Jia, G.; Hu, Y.; Fan, G.; Tsang, Y. H.; Li, Z.; Zou, Z., *Sustainable Energy Fuels* **2017**, *1*, 1875.

(2) (a) Lewis, N. S., *Science* **2016,** *351*, aad1920; (b) Jones, J.-P.; Prakash, G. K. S.; Olah, G. A., *Isr. J. Chem.* **2014,** *54*, 1451; (c) Zhan, Z.; Kobsiriphat, W.; Wilson, J. R.; Pillai, M.; Kim, I.; Barnett, S. A., *Energy Fuels* **2009,** *23*, 3089; (d) Peng, C.; Reid, G.; Wang, H.; Hu, P., *J. Chem. Phys.* **2017,** *147*, 030901; (e) Centi, G.; Perathoner, S., *ChemSusChem* **2010,** *3*, 195.

(3) (a) Costentin, C.; Robert, M.; Saveant, J.-M., *Chem. Soc. Rev.* **2013,** *42*, 2423; (b) Vasileff, A.; Zheng, Y.; Qiao, S. Z., *Adv. Energy. Mater.* **2017**, 1700759; (c) Hori, Y., Electrochemical CO_2 Reduction on Metal Electrodes. In *Modern Aspects of Electrochemistry*, Vayenas, C. G.; White, R. E.; Gamboa-Aldeco, M. E., Eds. Springer New York: New York, NY, 2008; pp 89; (d) Malik, K.; Singh, S.; Basu, S.; Verma, A., *WIREs Energy. Environ.* **2017,** *6*, e244; (e) Simakov, D. S. A., *Renewable Synthetic Fuels and Chemicals from Carbon Dioxide: Fundamentals, Catalysis, Design Considerations and Technological Challenges*. Springer International Publishing: Switzerland, 2017.

(4) (a) Zhang, L.; Zhao, Z.-J.; Gong, J., *Angew. Chem. Int. Ed.* **2017,** *56*, 11326; (b) Kortlever, R.; Shen, J.; Schouten, K. J. P.; Calle-Vallejo, F.; Koper, M. T. M., *J. Phys. Chem. Lett.* **2015,** *6*, 4073; (c) Lu, Q.; Jiao, F., *Nano Energy* **2016,** *29*, 439.

(5) (a) Whipple, D. T.; Kenis, P. J. A., *J. Chem. Phys. Lett.* **2010,** *1*, 3451; (b) Weng, Z.; Jiang, J.; Wu, Y.; Wu, Z.; Guo, X.; Materna, K. L.; Liu, W.; Batista, V. S.; Brudvig, G. W.; Wang, H., *J. Am. Chem. Soc.* **2016,** *138*, 8076; (c) Gattrell, M.; Gupta, N.; Co, A., *Energy Convers. Manage.* **2007,** *48*, 1255; (d) Kas, R.; Kortlever, R.; Milbrat, A.; Koper, M. T. M.; Mul, G.; Baltrusaitis, J., *Phys. Chem. Chem. Phys.* **2014,** *16*, 12194.

(6) (a) Li, C. W.; Ciston, J.; Kanan, M. W., *Nature* **2014,** *508*, 504; (b) Roberts, F. S.; Kuhl, K. P.; Nilsson, A., *Angew. Chem. Int. Ed.* **2015,** *54*, 5179; (c) Kuhl, K. P.; Cave, E. R.; Abram, D. N.; Jaramillo, T. F., *Energy Environ. Sci.* **2012,** *5*, 7050; (d) Ren, D.; Deng, Y.; Handoko, A. D.; Chen, C. S.; Malkhandi, S.; Yeo, B. S., *ACS. Catal.* **2015,** *5*, 2814.

(7) (a) Zheng, Y.; Jiao, Y.; Qiao, S. Z., *Adv. Mater.* **2015,** *27*, 5372; (b) Jiao, Y.; Zheng, Y.; Jaroniec, M. T.; Qiao, S. Z., *Chem. Soc. Rev.* **2015,** *44*, 2060.

(8) (a) Li, C. W.; Kanan, M. W., *J. Am. Chem. Soc.* **2012,** *134*, 7231; (b) Li, M.; Wang, J. J.; Li, P.; Chang, K.; Li, C. L.; Wang, T.; Jiang, B.; Zhang, H. B.; Liu, H. M.; Yamauchi, Y.; Umezawa, N.; Ye, J. H., *J. Mater. Chem. A* **2016,** *4*, 4776; (c) Huang, Y.; Handoko, A. D.; Hirunsit, P.; Yeo, B. S., *ACS. Catal.* **2017,** *7*, 1749; (d) Kim, D.; Xie, C. L.; Becknell, N.; Yu, Y.; Karamad, M.; Chan, K.; Crumlin, E. J.; Norskov, J. K.; Yang, P. D., *J. Am. Chem. Soc.* **2017,** *139*, 8329; (e) Li, Q.; Fu, J.; Zhu, W.; Chen, Z.; Shen, B.; Wu, L.; Xi, Z.; Wang, T.; Lu, G.; Zhu, J.-j.; Sun, S., *J. Am. Chem. Soc.* **2017,** *139*, 4290; (f) Bai, S.; Shao, Q.; Wang, P.; Dai, Q.; Wang, X.; Huang, X., *J. Am. Chem. Soc.* **2017,** *139*, 6827; (g) Hirunsit, P.; Soodsawang, W.; Limtrakul, J., *J. Phys. Chem. C* **2015,** *119*, 8238; (h) Ma, M.; Djanashvili, K.; Smith, W. A., *Angew. Chem. Int. Ed.* **2016,** *55*, 6680.

(9) (a) Nie, X. W.; Luo, W. J.; Janik, M. J.; Asthagiri, A., *J. Catal.* **2014,** *312*, 108; (b) Li, Y. W.; Chan, S. H.; Sun, Q., *Nanoscale* **2015,** *7*, 8663; (c) Xiao, H.; Cheng, T.; Goddard, W. A., *J. Am. Chem. Soc.* **2017,** *139*, 130; (d) Cheng, T.; Xiao, H.; Goddard, W. A., *J. Am. Chem. Soc.* **2016,** *138*, 13802; (e) Peterson, A. A.; Abild-Pedersen, F.; Studt, F.; Rossmeisl, J.; Norskov, J. K., *Energy Environ. Sci.* **2010,** *3*, 1311; (f) Liu, X. Y.; Xiao, J. P.; Peng, H. J.; Hong, X.; Chan, K.; Norskov, J. K., *Nat. Commun.* **2017,** *8*, 15438.

(10) (a) Rakowski Dubois, M.; Dubois, D. L., *Acc. Chem. Res.* **2009,** *42*, 1974; (b) Cheng, M. J.; Kwon, Y.; Head-Gordon, M.; Bell, A. T., *J. Phys. Chem. C* **2015,** *119*, 21345; (c) Back, S.; Lim, J.; Kim, N. Y.; Kim, Y. H.; Jung, Y., *Chem. Sci.* **2017,** *8*, 1090; (d) Shen, H. M.; Li, Y. W.; Sun, Q., *J. Phys. Chem. C* **2017,** *121*, 3963; (e) Li, Y. W.; Su, H. B.; Chan, S. H.; Sun, Q., *ACS. Catal.* **2015,** *5*, 6658; (f) Oh, Y.; Hu, X. L., *Chem. Soc. Rev.* **2013,** *42*, 2253; (g) Back, S.; Lim, J.; Kim, N.-Y.; Kim, Y. H.; Jung, Y., *Chem. Sci.* **2017,** *8*, 1090.

(11) Zheng, Y.; Jiao, Y.; Zhu, Y.; Cai, Q.; Vasileff, A.; Li, L. H.; Han, Y.; Chen, Y.; Qiao, S. Z., *J. Am. Chem. Soc.* **2017,** *139*, 3336.

(12) (a) Jiao, Y.; Zheng, Y.; Smith, S. C.; Du, A.; Zhu, Z., *ChemSusChem* **2014,** *7*, 435; (b) Tan, X.; Tahini, H. A.; Smith, S. C., *Curr. Opin. Electrochem.* **2017**, 10.1016/j.coelec.2017.08.006.

(13) Zheng, Y.; Jiao, Y.; Chen, J.; Liu, J.; Liang, J.; Du, A.; Zhang, W.; Zhu, Z.; Smith, S. C.; Jaroniec, M.; Lu, G. Q.; Qiao, S. Z., *J. Am. Chem. Soc.* **2011,** *133*, 20116.

(14) (a) Gowthaman, N. S. K.; Raj, M. A.; John, S. A., *ACS Sustainable Chem. Eng.* **2017,** *5*, 1648; (b) Liu, L.-L.; Chen, C.-P.; Zhao, L.-S.; Wang, Y.; Wang, X.-C., *Carbon* **2017,** *115*, 773.

(15) (a) Gao, P.; Li, S.; Bu, X.; Dang, S.; Liu, Z.; Wang, H.; Zhong, L.; Qiu, M.; Yang, C.; Cai, J.; Wei, W.; Sun, Y., *Nat. Chem.* **2017,** *9*, 1019; (b) Jiao, F.; Li, J.; Pan, X.; Xiao, J.; Li, H.; Ma, H.; Wei, M.; Pan, Y.; Zhou, Z.; Li, M.; Miao, S.; Li, J.; Zhu, Y.; Xiao, D.; He, T.; Yang, J.; Qi, F.; Fu, Q.; Bao, X., *Science* **2016,** *351*, 1065; (c) Lin, L.; Zhou, W.; Gao, R.; Yao, S.; Zhang, X.; Xu, W.; Zheng, S.; Jiang, Z.; Yu, Q.; Li, Y.-W.; Shi, C.; Wen, X.-D.; Ma, D., *Nature* **2017,** *544*, 80.

(16) (a) Kresse, G.; Hafner, J., *Phys. Rev. B* **1993,** *47*, 558; (b) Kresse, G.; Furthmüller, J., *Phys. Rev. B* **1996,** *54*, 11169; (c) Kresse, G.; Joubert, D., *Phys. Rev. B* **1999,** *59*, 1758; (d) Perdew, J. P.; Burke, K.; Ernzerhof, M., *Phys. Rev. Lett.* **1996,** *77*, 3865; (e) Perdew, J. P.; Burke, K.; Ernzerhof, M., *Phys. Rev. Lett.* **1997,** *78*, 1396.

(17) Tkatchenko, A.; Scheffler, M., *Phys. Rev. Lett.* **2009,** *102*, 073005.

(18)Durand, W. J.; Peterson, A. A.; Studt, F.; Abild-Pedersen, F.; Norskov, J. K., *Surf. Sci.* **2011,** *605*, 1354.

(19) Zhang, Y. J.; Sethuraman, V.; Michalsky, R.; Peterson, A. A., *ACS. Catal.* **2014,** *4*, 3742.

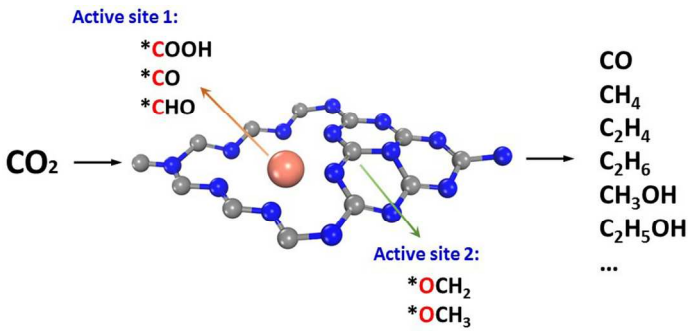
Active site 1:
*COOH
*CO
*CHO
CO2
Active site 2:
*OCH2
*OCH3
CO
CH4
C2H4
C2H6
CH3OH
C2H5OH
...